Berry curvature dipole in bilayer graphene with interlayer sliding

Jie Pan, Haibo Xie, Pengyuan Shi, Xiaoyu Wang, Lihao Zhang, and Zhe Wang*

MOE Key Laboratory for Nonequilibrium Synthesis and Modulation of Condensed Matter, Shaanxi Province Key Laboratory of Advanced Materials and Mesoscopic Physics, School of Physics, Xi'an Jiaotong University, Xi'an 710049, China

(Received 4 December 2023; revised 23 January 2024; accepted 24 January 2024; published 14 February 2024)

Lowering lattice symmetry plays a pivotal role in generating a nonzero Berry curvature dipole. In this work, we demonstrate that introducing an interlayer sliding in bilayer graphene effectively breaks the inherent threefold rotational symmetry, thus giving rise to a nonzero Berry curvature dipole. Our numerical simulations also reveal the magnitude of the Berry curvature dipole can be further tuned by various parameters, including interlayer sliding distances and directions, as well as interlayer potential differences. We show even a tiny sliding distance of 0.02 nm can lead to a substantial Berry curvature dipole of about 10 nm in bilayer graphene, which is comparable to the values measured in transition metal dichalcogenides (TMDCs). Our work represents a new way to manipulate the topological properties of bilayer graphene, and this methodology can be extended into other two-dimensional systems, such as TMDCs with threefold rotational symmetry.

DOI: 10.1103/PhysRevB.109.075415

I. INTRODUCTION

Physical properties of two-dimensional (2D) materials can be significantly influenced by interlayer stacking, which is determined by two critical parameters: the twisting angle and sliding vector. In recent years, manipulating twisting angles has proven to be an effective method for modulating electronic [1,2], magnetic [3–5], and optical [6–8] properties of 2D materials. A striking example is magic-angle bilayer graphene, which is characterized by a specific twisting angle (approximately 1.1°) between its two carbon layers. This system has been shown to exhibit a wide range of novel physical phenomena, including Mott transition [1], unconventional superconductivity [2,9], ferromagnetism [10], topological physics [11,12], and so on. On the other hand, exploration of the effects of interlayer sliding, i.e., introducing sliding between adjacent carbon layers, is still in its early stages. Previous research on bilayer graphene with interlayer sliding has primarily focused on the theoretical calculation of its band structure [13–16], with limited attention given to the exploration of symmetry-related topological properties. In this work, we demonstrate that interlayer sliding effectively breaks the threefold rotational symmetry of bilayer graphene's carbon lattices, leading to significant modifications in its topological properties. Specifically, it results in the emergence of a nonzero and tunable Berry curvature dipole.

The Berry curvature dipole, defined as the first moment of the Berry curvature in momentum (k) space, has recently gained prominence as an intrinsic mechanism underlying the nonlinear Hall effect, as demonstrated in the work by Sodemann and Fu [17]. The nonlinear Hall effect can manifest itself in systems possessing time-reversal symmetry [18,19], which distinguishes it from the conventional linear Hall effect. It is pertinent to systems with lower spatial symmetries. In 2D systems, the observation of nonlinear Hall effect is contingent upon the existence of mirror symmetry as the sole spatial symmetry [17,20]. Since the theoretical prediction of nonlinear Hall effect, this phenomenon has been subsequently verified in various 2D systems, such as intrinsically low-symmetry materials including bilayer and few-layer WTe_2 [18,19,21]. Besides these, in symmetric 2D transition metal dichalcogenides (TMDCs), such as MoS_2 and WSe_2, a nonzero Berry curvature can be induced by reducing spatial symmetry, often by breaking threefold rotational symmetry through methods like strain engineering in monolayer MoS_2 [22] and twisted WSe_2 [23,24]. For naturally high symmetric graphene systems, several theoretical approaches have been proposed to lower the lattice symmetry and generate a nonzero Berry curvature dipole, such as inducing a uniaxial strain in both monolayer and bilayer graphene [20], as well as exploring strained twisted bilayer graphene systems [25,26]. Recent experimental work has further confirmed the existence of a nonzero Berry curvature dipole in systems of twisted [27] and strained bilayer graphene [28], and twisted double bilayer graphene [29], as verified by the observation of nonlinear Hall effect. Instead of strain engineering and twisting angles, we present an innovative approach, namely interlayer sliding, in this study to lower the lattice symmetry of bilayer graphene and achieve nonzero Berry curvature dipole.

It is noteworthy that the interlayer sliding is easily accessible due to the weak van der Waals interactions governing interlayer coupling in various 2D materials. Recent experimental observations have shown that interlayer sliding can induce changes in electric polarization in 2D ferroelectric materials, such as manually parallel stacked BN [30,31]. In the case of few-layer graphene systems, interlayer sliding has been observed when graphene is placed on BN steps [32], and the sliding distance was found to be around 0.3 nm ($\sim 2a$, with $a = 0.142$ nm being carbon-carbon bond length). In

*zhe.wang@xjtu.edu.cn

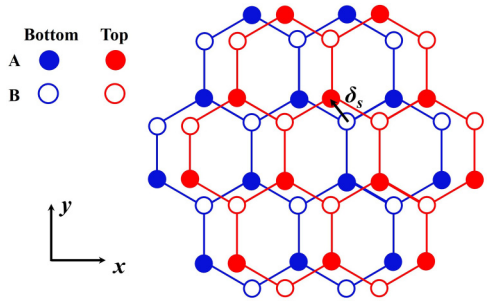

FIG. 1. Cartoon image of bilayer graphene with interlayer sliding. Here the blue (red) lattice represents the bottom (top) layer of bilayer graphene and the solid (open) circles stand for carbon A(B) sublattice; the dashed line connects four different types of carbon atoms in a unitcell.

this work, we establish the effective tunability of topological properties through the manipulation of interlayer sliding. It is demonstrated that even a tiny interlayer sliding of 0.02 nm ($\sim 0.15a$) between different carbon layers of bilayer graphene can trigger the emergence of a significant Berry curvature dipole of 10 nm ($\sim 76a$). This suggests that interlayer sliding is a powerful tool for tailoring the topological properties in graphene. Moreover, this approach can be extended to other 2D material systems with threefold rotational symmetry, such as TMDCs.

In the subsequent sections, we begin by introducing the interlayer sliding model and simulation methods in Sec. II. We delve into the simulation results, focusing on the distributions of Berry curvature and Berry curvature dipole density under interlayer sliding in Sec. III. We investigate the integrated Berry curvature dipole as a function of Fermi energy, exploring various sliding vectors and interlayer potential differences. A brief summary is included in Sec. IV.

II. SIMULATION METHODS

Among various stacking modes in bilayer graphene, AB (Bernal) stacking is the most thermodynamically stable configuration. Therefore, in this study, we commence with the AB stacking mode as the reference structure. To model interlayer sliding, we introduce a sliding vector $\boldsymbol{\delta}_s = (\delta x, \delta y)$, as illustrated in Fig. 1. We express sliding distances in terms of the carbon-carbon bond length a (=0.142 nm). Berry curvature and its dipole are expressed in the unit of a^2 and a, respectively. The adjacent carbon layer separation is given by h (=0.335 nm).

We employ the tight-binding model to simulate the electronic properties of bilayer graphene with interlayer sliding. The Hamiltonian, expressed in the basis of $(A_{\text{bottom}}, B_{\text{bottom}}, A_{\text{top}}, B_{\text{top}})$, is as follows:

$$H = \begin{pmatrix} H_{\text{intra}}(V) & H_{\text{inter}}(\boldsymbol{\delta}_s) \\ H^{\dagger}_{\text{inter}}(\boldsymbol{\delta}_s) & H_{\text{intra}}(-V) \end{pmatrix}, \tag{1}$$

where the intralayer hopping term is denoted by H_{intra} and interlayer hopping term H_{inter}. The intralayer hopping is independent of sliding vector $\boldsymbol{\delta}_s$ and is expressed as

$$H_{\text{intra}}(\pm V) = \begin{pmatrix} \pm V & \sum_i t(\boldsymbol{\delta}_i, 0) e^{i\mathbf{k}\cdot\boldsymbol{\delta}_i} \\ \sum_i t(\boldsymbol{\delta}_i, 0) e^{-i\mathbf{k}\cdot\boldsymbol{\delta}_i} & \pm V \end{pmatrix}, \tag{2}$$

where $\pm V$ denotes the interlayer potential differences, and the summation over $\boldsymbol{\delta}_i$ in the off-diagonal terms covers all the nearest neighbors, including $\boldsymbol{\delta}_1 = (\sqrt{3}/2, -1/2)a$, $\boldsymbol{\delta}_2 = (-\sqrt{3}/2, -1/2)a$, and $\boldsymbol{\delta}_3 = (0, 1)a$; the hopping energy $t(\boldsymbol{\delta}_i, 0)$ is a function of in-plane carbon atom separation $\boldsymbol{\delta}_i$ and out-of-plane separation (which is zero in intralayer hopping case). The interlayer hopping term, on the other hand, is expressed as

$$H_{\text{inter}} = \begin{pmatrix} \sum_i t(\boldsymbol{\delta}_s + \boldsymbol{\delta}_i, h) e^{i\mathbf{k}\cdot(\boldsymbol{\delta}_s + \boldsymbol{\delta}_i)} & \sum_i t(\boldsymbol{\delta}_s - \boldsymbol{\delta}_i, h) e^{i\mathbf{k}\cdot(\boldsymbol{\delta}_s - \boldsymbol{\delta}_i)} \\ t(\boldsymbol{\delta}_s, h) e^{i\mathbf{k}\cdot\boldsymbol{\delta}_s} & \sum_i t(\boldsymbol{\delta}_s + \boldsymbol{\delta}_i, h) e^{i\mathbf{k}\cdot(\boldsymbol{\delta}_s + \boldsymbol{\delta}_i)} \end{pmatrix}; \tag{3}$$

both the hopping energy t and phase factors are $\boldsymbol{\delta}_s$ dependent, in contrast to the intralayer hopping term. It's worth noting that the magnitude of sliding distance δ_s is limited to a small portion of a, therefore the interlayer sliding vector $\boldsymbol{\delta}_s$ simply changes hopping energy and phase, but the numbers of nearest neighbor hoppings remain the same in this work.

To model the hopping energy variation under interlayer sliding, we apply the widely used relation between hopping energy magnitude and arbitrary carbon atom separations [33–36],

$$t(\boldsymbol{\delta}, z) = V_\pi e^{-(d-a)/r_0} \sin^2\alpha + V_\sigma e^{-(d-h)/r_0} \cos^2\alpha, \tag{4}$$

where $V_\pi = -t$, $V_\sigma = 0.18t$, $r_0 = 0.0453$ nm, d is the separation between two atoms $d = \sqrt{|\boldsymbol{\delta}|^2 + z^2}$, and α is the angle between displacement vector $(\boldsymbol{\delta}, z)$ and the z axis. For a given sliding vector $\boldsymbol{\delta}_s$, we can substitute Eq. (4) into Eqs. (1)–(3), thereby allowing us to numerically determine the tight-binding Hamiltonian.

III. RESULTS AND DISCUSSIONS

A. Berry curvature and dipole density distributions

With the Hamiltonian established as in Eq. (1), we can numerically compute the Berry curvature distribution in the k space. For a 4×4 matrix, there will be four bands. Here we focus on the first conduction band, and the Berry curvature is given by [37]

$$\Omega_3 = i \frac{\sum_{j\neq 3} [\langle\phi_j|\partial H/\partial k_x|\phi_3\rangle\langle\phi_3|\partial H/\partial k_y|\phi_j\rangle - \text{c.c.}]}{(\varepsilon_3 - \varepsilon_j)^2}, \tag{5}$$

where ϕ_j and ε_j denote the jth eigenvectors and eigenvalues, respectively; we arrange the eigenvalues in ascending order and therefore index $j = 3$ corresponds to the first conduction band. We set the interlayer potential difference $V = 0.03t$, approximately 80 meV, a value readily attainable by applying a displacement field using dual gates [38,39]. We first set $\boldsymbol{\delta}_s$ to be along the y direction. Berry curvature distributions under

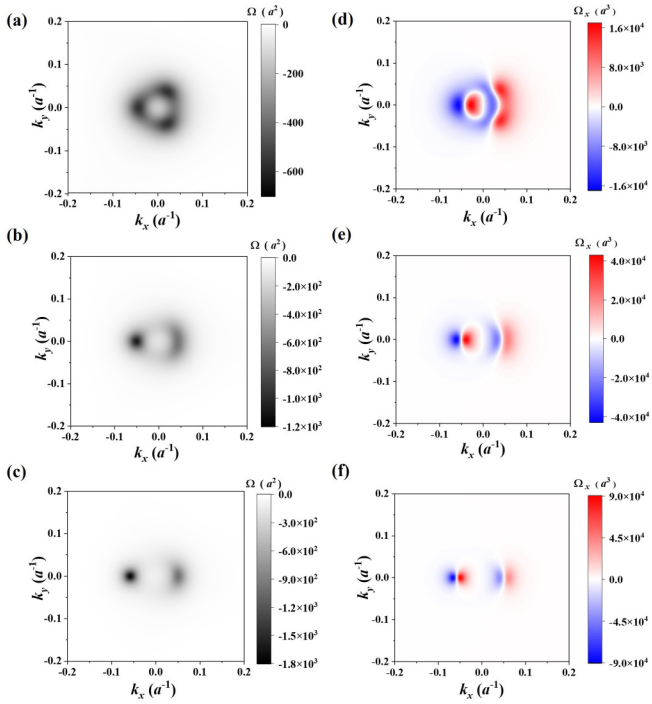

FIG. 2. Simulated Berry curvature and Berry curvature dipole density in the k space. The potential difference between two layers is set to be $V = 0.03t$, with the sliding vector oriented along the y direction. The Berry curvature and Berry curvature dipole density distributions are plotted with three different sliding distances: (a) and (d) 0, (b) and (e) $0.08a$, and (c) and (f) $0.15a$.

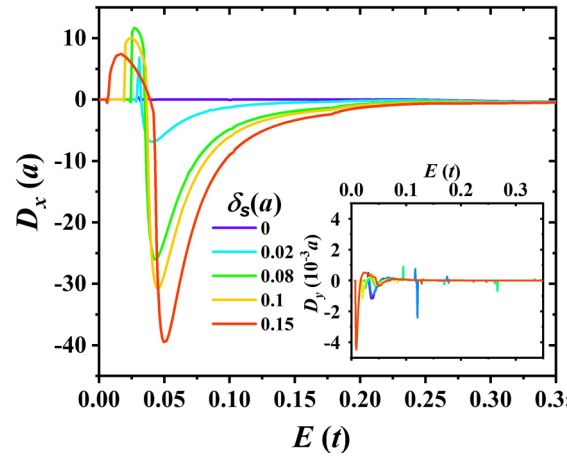

FIG. 3. Simulated Berry curvature dipole D_x in the unit of a as a function of Fermi energy for different sliding distances. The potential difference V is fixed at $0.03t$ with sliding vector along the y axis. The sliding distance varies from 0 to $0.15a$. Inset is the simulated Berry curvature dipole D_y which is consistently zero due to the mirror symmetry of the Berry curvature distribution.

different sliding distances are plotted in Figs. 2(a) for $\delta_s = 0$, 2(b) for $\delta_s = 0.08a$, and 2(c) for $\delta_s = 0.15a$.

The simulated Berry curvature distribution of the AB stacking ($\delta_s = 0$) case is presented in Fig. 2(a). In this simulation, k is chosen to be around Dirac point K. It is seen that the Berry curvature distribution exhibits a distinctive threefold rotational symmetry around the K point, a characteristic stemming from the threefold rotational symmetry of carbon lattice. The three nonzero Berry curvature pots are related to the Lifshitz transition but slightly different from Ref. [20] due to different choices of hopping parametrization. However, when interlayer sliding occurs along the y axis, this threefold rotational symmetry of lattice is broken, as evident in Figs. 2(b) and 2(c). It's important to note that a mirror symmetry in the lattice structure remains intact (particularly when sliding parallel to the y axis). This can be easily verified by considering the y direction interlayer sliding in Fig. 1; the quadrilateral formed by the four carbon atoms would become an isosceles trapezoid with the x axis to be the mirror symmetry line. Consequently, the periodic part of the Bloch wavefunciton must satisfy $u(k_x, k_y) = u(k_x, -k_y)$, thereby leading to the Berry curvature also exhibiting mirror symmetry, $\Omega(k_x, k_y) = \Omega(k_x, -k_y)$, as shown in Fig. 2. Based on the calculated Berry curvature distribution, we can readily evaluate the Berry curvature dipole density using $\Omega_x = \partial\Omega/\partial k_x$. The calculated dipole density is summarized in Figs. 2(d)–2(f) for $\delta_s = 0$, 0.08, and $0.15a$, respectively. It is shown that the Berry curvature dipole density centered around the Berry curvature dips observed in Figs. 2(a)–2(c), with positive and negative values in proximity to each other. As the interlayer sliding distance increases, the maximum absolute value of dipole density also increases. It should be noted that we have only calculated the x component of dipole density, due to the facts that the y component cancels out when calculating the net Berry curvature dipole for any fixed Fermi energy.

B. Berry curvature dipole with y-direction interlayer sliding

For a given Fermi energy, Berry curvature dipole D_x should be obtained by integrating Ω_x over the k space of occupied states [17,20] as follows:

$$D_x = \int_k f(\Omega_x), \tag{6}$$

where f is the Fermi-Dirac distribution and for our calculations we assume the zero-temperature limit, making f essentially a heaviside step function. To perform this integration, the knowledge of electronic bandstructure of the system is also required. The integrated dipole D_x is shown in Fig. 3. In line with the conditions in Fig. 2, we keep the interlayer potential difference $V = 0.03t$ and the sliding vector along the y direction with distance varied from 0 to $0.15a$. It should also be noted that the time reversal symmetry requires Berry curvature to be an odd function in k space (e.g., antisymmetric between K and K' valleys). Consequently, the Berry curvature dipole density emerges as an even function. Therefore, when integrated over the entire k space, the Berry curvature dipole doubles rather than canceling out.

The D_x-E curve exhibits distinct characteristics: it starts with a positive value, sharply declines to a negative value, and eventually approaches zero as the Fermi energy increases. For $\delta_s = 0.15a$, the maximum absolute value of Berry curvature can reach up to $40a$ (around 6 nm), which is comparable with

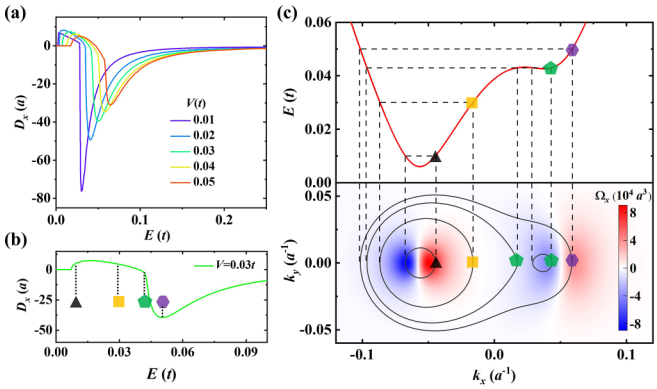

FIG. 4. (a) Simulated Berry curvature dipole D_x in the unit of a as a function of Fermi energy for various interlayer potential differences. The sliding vector is set to be $(0, 0.15a)$ and the potential difference V varies from 0.01 to $0.05t$. For the $V = 0.03t$ case, (b) depicts the enlarged image of D_x as a function of Fermi energy, while (c) illustrates the bandstructure with $k_y = 0$ (upper panel), Ω_x (indicated by varying colors), and isoenergy lines in k space (lower panel). Four representative energy point in (b) and (c)—black triangle ($0.01t$), yellow square ($0.03t$), green pentagon ($0.043t$) and purple hexagon ($0.05t$)—are selected for detailed discussions.

that measured in WTe_2 [19]. We later demonstrate that this value can increase further with a weaker interlayer potential difference. As the sliding distance increases, there is a notable decrease in the onset energy of positive Berry curvature dipole. This reduction can be attributed to the narrowing of the band gap resulting from interlayer sliding, similar to what was reported in Ref. [15]. Moreover, we have also calculated the y component of Berry curvature dipole D_y, which consistently yields values close to zero ($<10^{-4}D_x$), as shown in the inset of Fig. 3. This verification underscores the accuracy of our numerical results.

Berry curvature dipole D_x as a function of Fermi energy for different interlayer potential differences V, ranging from $0.01t$ to $0.05t$, is summarized in Fig. 4(a), where the sliding vector is fixed at $\boldsymbol{\delta_s} = (0, 0.15a)$. It can be seen that the onset energy of positive D_x increases with V due to the widening of band gaps. Additionally, the maximum absolute value of Berry curvature density D_x increases as V decreases, consistent with what was reported in Ref. [20]. For $V = 0.01t$, Berry curvature dipole with a magnitude of $76a$ (around 10 nm) is obtained. This behavior arises because the Berry curvature is confined to a more compact k space when the potential difference V is smaller, leading to a larger Berry curvature dipole within a narrower energy range.

To gain further insight to the characteristics of nonzero Berry curvature dipole as a function of Fermi energy, we take the case of $V = 0.03t$ and $\boldsymbol{\delta_s} = (0, 0.15a)$ as an example to discuss in detail. The energy dependency of Berry curvature dipole D_x is shown in Fig. 4(b). Four representative energy points—black triangle ($0.01t$), yellow square ($0.03t$), green pentagon ($0.043t$), and purple hexagon ($0.05t$)—are selected to elucidate how the Fermi level influences D_x. Notably, there are two local energy minima, which can be easily identified from the bandstructure in the upper panel of Fig. 4(c). When the Fermi level is tuned from zero to the black triangle point, the left Berry curvature pot is encountered, where the positive Ω_x (in red) slightly dominates, explaining the onset of positive D_x. Increasing the Fermi level to the yellow square point results in a significant cancellation between negative and positive Ω_x, leading to the decrease of D_x. Upon reaching the green pentagon point, the Fermi surface encompasses the additional Berry curvature pot on the right, where the negative Ω_x (in blue) dominates, results in a sharp drop of Berry curvature dipole D_x to a negative value. As the Fermi level is tuned to the purple hexagon point, where the Fermi surface deviation induces an equal amount of positive and negative Ω_x, a maximum absolute value of D_x is obtained. The appearance of a maximum magnitude of D_x is observed in various systems, including strained graphene and WSe_2 [20,24,26]. It is interesting to note that the sign change of the Berry curvature dipole has been observed to be associated with topological phase transitions in previous study [24]. In our case, this behavior is linked to the Fermi surface encompassing an additional Berry curvature pot, and nonlinear Hall effect measurements could potentially be employed to detect complex Lifshitz transitions in bilayer graphene with interlayer slidings.

C. Sliding angular dependence of Berry curvature dipole

In this subsection, we explore the angular dependence of the Berry curvature dipole under interlayer sliding. We introduce a variable θ, which denotes the angle between the sliding vector $\boldsymbol{\delta_s}$ and the x axis. Up to this point, our investigation has been limited to interlayer sliding exclusively along the y axis (corresponding to the $\theta = \pi/2$ case). However, in this subsection, we extend our examination to encompass a wide range of θ values, spanning from 0 to 2π, with sliding distance fixed at $0.08a$ and the interlayer potential difference fixed at $0.03t$. It's important to note that when sliding along arbitrary directions, the k_y axis mirror symmetry of the Berry curvature $\Omega(k_x, k_y)$ is no longer applicable. Consequently, both the x component (D_x) and the y component (D_y) of the Berry curvature dipoles will be subject to investigation in this subsection.

By employing the same methodology as described earlier, we can compute both D_x and D_y for various sliding angles and Fermi energies. In Figs. 5(a) and 5(b), we present the Berry curvature dipole $D_{x(y)}$ as a function of Fermi energy (on the radial axis) and sliding direction θ (on the angular axis). For D_x, we observe that the maximum absolute value is attained when sliding occurs along the $\pm y$ axes, corresponding to $\theta = \pm\pi/2$. Additionally, we notice the onset of positive Berry curvature dipole values switching to negative values when sliding along $\theta = \pi/2$, which aligns with our previous observations in Figs. 3 and 4. Notably, a symmetric relation emerges, expressed as $D_x(\theta) = D_x(\pi - \theta)$. In contrast, for the D_y component, we observe an antisymmetric relation, specifically $D_y(\theta) = -D_y(\pi - \theta)$. When we set $\theta = \pi/2$, we obtain $D_y(\pi/2) = 0$, which is consistent with Fig. 5(b) and also aligns with the mirror symmetry analysis presented in Sec. III A.

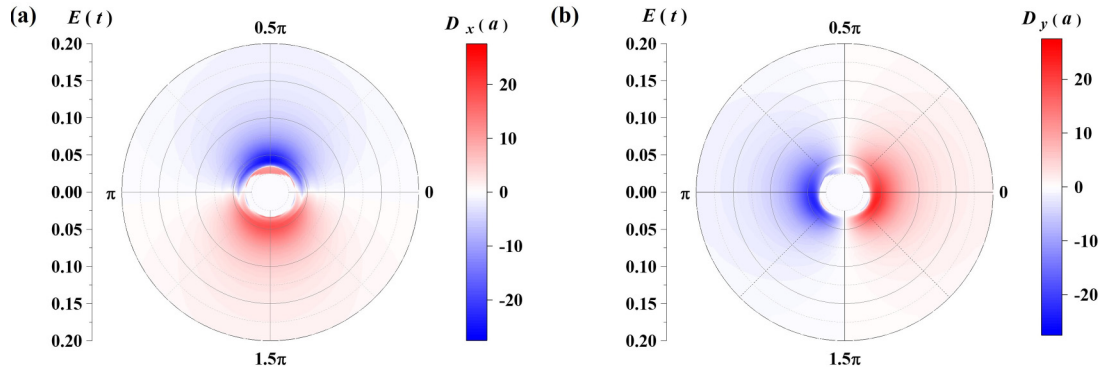

FIG. 5. Berry curvature dipole $D_{x(y)}$ plotted as a function of Fermi energy and sliding angle in (a) and (b). The sliding distance is fixed at $0.08a$ and the interlayer potential difference is set to be $0.03t$.

To elucidate the (anti)symmetric observation of Berry curvature dipole $D_{x(y)}$ with respect to $\theta = \pi/2$ (i.e., y axis), we demonstrate two cases with symmetric sliding angles: $\theta_1 = 2\pi/3$ and $\theta_2 = \pi/3$, as shown by the sliding vector $\boldsymbol{\delta}_{s1(2)}$ in Figs. 6(a) and 6(b). In both cases, the four carbon atoms in the unit cell are represented by the dashed quadrilateral as shown in Figs. 6(a) and 6(b). It becomes evident that these two cases are symmetric with each other when considering the mirror line symmetry of the x axis. Therefore, one expects that the periodic part of Bloch wavefunction must satisfy the relationship $u_1(k_x, k_y) = u_2(k_x, -k_y)$, where subsets 1 and 2 represent the two cases with symmetric sliding angles in Figs. 6(a) and 6(b). It follows that the Berry curvature distribution should obey $\Omega_1(k_x, k_y) = \Omega_2(k_x, -k_y)$, which is numerically verified in Figs. 6(c) and 6(d). As a result, we can obtain the symmetric relation for the x component of Berry curvature dipole $D_x(\theta) = D_x(\pi - \theta)$ and the antisymmetric relation for y component $D_y(\theta) = -D_y(\pi - \theta)$.

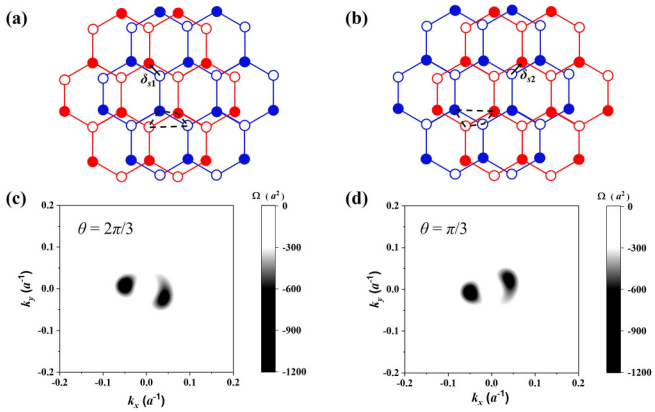

FIG. 6. Demonstration of interlayer sliding along (a) $\theta = 2\pi/3$ and (b) $\theta = \pi/3$; these two cases are symmetric with respect to mirror reflection along the y axis. Berry curvature simulation results for fixed sliding distance $0.08a$ and interlayer potential difference $0.03t$ for (c) $\theta = 2\pi/3$ and (d) $\theta = \pi/3$. These two cases are mirror symmetric to each other with respect to $k_y = 0$.

Our examination of the angular dependence of the Berry curvature dipole reveals that a nonzero Berry curvature can be achieved by introducing interlayer sliding along arbitrary directions in a gapped bilayer graphene system. Notably, the properties of the Berry curvature dipole are strongly influenced by the spatial symmetry of the carbon lattice. In addition to its substantial magnitude, our simulation results vividly demonstrate that the Berry curvature dipole can be finely tuned by various parameters, including sliding distances, sliding directions, and perpendicular displacement fields (potential differences). Consequently, we anticipate the emergence of a robust nonlinear Hall effect signal in bilayer graphene systems subject to interlayer sliding, offering a high degree of tunability.

IV. SUMMARY

In summary, our study has demonstrated that the introduction of interlayer sliding in bilayer graphene can result in a nonzero Berry curvature dipole due to the breakdown of threefold rotational symmetry. Our numerical simulations have revealed that this nonzero Berry curvature can be finely tuned by adjusting interlayer potential differences, sliding distances, and directions. Remarkably, even a tiny sliding distance of 0.02 nm can yield a substantial Berry curvature dipole on the order of 10 nm. Our work presents an innovative approach to control the Berry curvature dipole in graphene systems, and we anticipate that this method can be extended to other 2D materials, such as TMDCs with inherent threefold rotational symmetry, for effective engineering of their topological properties.

ACKNOWLEDGMENTS

J.P. would like to thank Wenbin Rui for helpful discussions. This work is financially supported by the National Natural Science Foundation of China (Grants No. 12304232 and No. 12374121), Shaanxi Fundamental Science Research Project for Mathematics and Physics (22JSY026), the Fundamental Research Funds for the Central Universities.

[1] Y. Cao, V. Fatemi, A. Demir, S. Fang, S. L. Tomarken, J. Y. Luo, J. D. Sanchez-Yamagishi, K. Watanabe, T. Taniguchi, E. Kaxiras, R. C. Ashoori, and P. Jarillo-Herrero, Correlated insulator behaviour at half-filling in magic-angle graphene superlattices, Nature (London) **556**, 80 (2018).

[2] Y. Cao, V. Fatemi, S. Fang, K. Watanabe, T. Taniguchi, E. Kaxiras, and P. Jarillo-Herrero, Unconventional superconductivity in magic-angle graphene superlattices, Nature (London) **556**, 43 (2018).

[3] T. Song, Q.-C. Sun, E. Anderson, C. Wang, J. Qian, T. Taniguchi, K. Watanabe, M. A. McGuire, R. Stohr, D. Xiao, T. Cao, J. Wrachtrup, and X. Xu, Direct visualization of magnetic domains and moire magnetism in twisted 2d magnets, Science **374**, 1140 (2021).

[4] Y. Xu, A. Ray, Y.-T. Shao, S. Jiang, K. Lee, D. Weber, J. E. Goldberger, K. Watanabe, T. Taniguchi, D. A. Muller, K. F. Mak, and J. Shan, Coexisting ferromagnetic-antiferromagnetic state in twisted bilayer CrI_3, Nat. Nanotechnol. **17**, 143 (2022).

[5] H. Xie, X. Luo, G. Ye, Z. Ye, H. Ge, S. H. Sung, E. Rennich, S. Yan, Y. Fu, S. Tian, H. Lei, R. Hovden, K. Sun, R. He, and L. Zhao, Twist engineering of the two-dimensional magnetism in double bilayer chromium triiodide homostructures, Nat. Phys. **18**, 30 (2022).

[6] K. Tran, G. Moody, F. Wu, X. Lu, J. Choi, K. Kim, A. Rai, D. A. Sanchez, J. Quan, A. Singh, J. Embley, A. Zepeda, M. Campbell, T. Autry, T. Taniguchi, K. Watanabe, N. Lu, S. K. Banerjee, K. L. Silverman, S. Kim, E. Tutuc, L. Yang, A. H. MacDonald, and X. Li, Evidence for moire excitons in van der waals heterostructures, Nature (London) **567**, 71 (2019).

[7] E. M. Alexeev, D. A. Ruiz-Tijerina, M. Danovich, M. J. Hamer, D. J. Terry, P. K. Nayak, S. Ahn, S. Pak, J. Lee, J. I. Sohn, M. R. Molas, M. Koperski, K. Watanabe, T. Taniguchi, K. S. Novoselov, R. V. Gorbachev, H. S. Shin, V. I. Fal'ko, and A. I. Tartakovskii, Resonantly hybridized excitons in moire superlattices in van der waals heterostructures, Nature (London) **567**, 81 (2019).

[8] G. Hu, Q. Ou, G. Si, Y. Wu, J. Wu, Z. Dai, A. Krasnok, Y. Mazor, Q. Zhang, Q. Bao, C.-W. Qiu, and A. Alu, Topological polaritons and photonic magic angles in twisted α-MoO_3 bilayers, Nature (London) **582**, 209 (2020).

[9] H. Kim, Y. Choi, C. Lewandowski, A. Thomson, Y. Zhang, R. Polski, K. Watanabe, T. Taniguchi, J. Alicea, and S. Nadj-Perge, Evidence for unconventional superconductivity in twisted trilayer graphene, Nature (London) **606**, 494 (2022).

[10] A. L. Sharpe, E. J. Fox, A. W. Barnard, J. Finney, K. Watanabe, T. Taniguchi, M. A. Kastner, and D. Goldhaber-Gordon, Emergent ferromagnetism near three-quarters filling in twisted bilayer graphene, Science **365**, 605 (2019).

[11] Y. Choi, H. Kim, Y. Peng, A. Thomson, C. Lewandowski, R. Polski, Y. Zhang, H. S. Arora, K. Watanabe, T. Taniguchi, J. Alicea, and S. Nadj-Perge, Correlation-driven topological phases in magic-angle twisted bilayer graphene, Nature (London) **589**, 536 (2021).

[12] Y. Saito, J. Ge, L. Rademaker, K. Watanabe, T. Taniguchi, D. A. Abanin, and A. F. Young, Hofstadter subband ferromagnetism and symmetry-broken chern insulators in twisted bilayer graphene, Nat. Phys. **17**, 478 (2021).

[13] Y.-W. Son, M. L. Cohen, and S. G. Louie, Energy gaps in graphene nanoribbons, Phys. Rev. Lett. **97**, 216803 (2006).

[14] C. Park, J. Ryou, S. Hong, B. G. Sumpter, G. Kim, and M. Yoon, Electronic properties of bilayer graphene strongly coupled to interlayer stacking and an external electric field, Phys. Rev. Lett. **115**, 015502 (2015).

[15] K. W. Lee and C. E. Lee, Extreme sensitivity of the electric-field-induced band gap to the electronic topological transition in sliding bilayer graphene, Sci. Rep. **5**, 17490 (2015).

[16] V. N. Do, Proof for the electronic band crossing in sliding bilayer graphene, Phys. Rev. B **104**, 205121 (2021).

[17] I. Sodemann and L. Fu, Quantum nonlinear hall effect induced by berry curvature dipole in time-reversal invariant materials, Phys. Rev. Lett. **115**, 216806 (2015).

[18] K. Kang, T. Li, E. Sohn, J. Shan, and K. F. Mak, Nonlinear anomalous hall effect in few-layer WTe_2, Nat. Mater. **18**, 324 (2019).

[19] Q. Ma, S.-Y. Xu, H. Shen, D. MacNeill, V. Fatemi, T.-R. Chang, A. M. Mier Valdivia, S. Wu, Z. Du, C.-H. Hsu, S. Fang, Q. D. Gibson, K. Watanabe, T. Taniguchi, R. J. Cava, E. Kaxiras, H.-Z. Lu, H. Lin, L. Fu, N. Gedik, and P. Jarillo-Herrero, Observation of the nonlinear hall effect under time-reversal-symmetric conditions, Nature (London) **565**, 337 (2019).

[20] R. Battilomo, N. Scopigno, and C. Ortix, Berry curvature dipole in strained graphene: A fermi surface warping effect, Phys. Rev. Lett. **123**, 196403 (2019).

[21] Z. Z. Du, C. M. Wang, H.-Z. Lu, and X. C. Xie, Band signatures for strong nonlinear hall effect in bilayer WTe_2, Phys. Rev. Lett. **121**, 266601 (2018).

[22] J. Son, K.-H. Kim, Y. H. Ahn, H.-W. Lee, and J. Lee, Strain engineering of the berry curvature dipole and valley magnetization in monolayer MoS_2, Phys. Rev. Lett. **123**, 036806 (2019).

[23] M. Huang, Z. Wu, J. Hu, X. Cai, E. Li, L. An, X. Feng, Z. Ye, N. Lin, K. T. Law, and N. Wang, Giant nonlinear Hall effect in twisted bilayer Wse_2, Natl. Sci. Rev. **10**, nwac232 (2022).

[24] J.-X. Hu, C.-P. Zhang, Y.-M. Xie, and K. T. Law, Nonlinear hall effects in strained twisted bilayer WSe_2, Commun. Phys. **5**, 255 (2022).

[25] P. A. Pantaleón, T. Low, and F. Guinea, Tunable large berry dipole in strained twisted bilayer graphene, Phys. Rev. B **103**, 205403 (2021).

[26] C.-P. Zhang, J. Xiao, B. T. Zhou, J.-X. Hu, Y.-M. Xie, B. Yan, and K. T. Law, Giant nonlinear hall effect in strained twisted bilayer graphene, Phys. Rev. B **106**, L041111 (2022).

[27] M. Huang, Z. Wu, X. Zhang, X. Feng, Z. Zhou, S. Wang, Y. Chen, C. Cheng, K. Sun, Z. Y. Meng, and N. Wang, Intrinsic nonlinear hall effect and gate-switchable berry curvature sliding in twisted bilayer graphene, Phys. Rev. Lett. **131**, 066301 (2023).

[28] S.-C. Ho, C.-H. Chang, Y.-C. Hsieh, S.-T. Lo, B. Huang, T.-H.-Y. Vu, C. Ortix, and T.-M. Chen, Hall effects in artificially corrugated bilayer graphene without breaking time-reversal symmetry, Nat. Electron. **4**, 116 (2021).

[29] S. Sinha, P. C. Adak, A. Chakraborty, K. Das, K. Debnath, L. D. V. Sangani, K. Watanabe, T. Taniguchi, U. V. Waghmare, A. Agarwal, and M. M. Deshmukh, Berry curvature dipole senses topological transition in a moiré superlattice, Nat. Phys. **18**, 765 (2022).

[30] M. V. Stern, Y. Waschitz, W. Cao, I. Nevo, K. Watanabe, T. Taniguchi, E. Sela, M. Urbakh, O. Hod, and M. B. Shalom, Interfacial ferroelectricity by van der waals sliding, Science **372**, 1462 (2021).

[31] K. Yasuda, X. Wang, K. Watanabe, T. Taniguchi, and P. Jarillo-Herrero, Stacking-engineered ferroelectricity in bilayer boron nitride, Science **372**, 1458 (2021).

[32] E. Han, J. Yu, E. Annevelink, J. Son, D. A. Kang, K. Watanabe, T. Taniguchi, E. Ertekin, P. Y. Huang, and A. M. van der Zande, Ultrasoft slip-mediated bending in few-layer graphene, Nat. Mater. **19**, 305 (2020).

[33] T. Nakanishi and T. Ando, Conductance of crossed carbon nanotubes, J. Phys. Soc. Jpn. **70**, 1647 (2001).

[34] S. Uryu, Electronic states and quantum transport in double-wall carbon nanotubes, Phys. Rev. B **69**, 075402 (2004).

[35] G. Trambly de Laissardière, D. Mayou, and L. Magaud, Localization of dirac electrons in rotated graphene bilayers, Nano Lett. **10**, 804 (2010).

[36] P. Moon and M. Koshino, Energy spectrum and quantum hall effect in twisted bilayer graphene, Phys. Rev. B **85**, 195458 (2012).

[37] D. Xiao, M.-C. Chang, and Q. Niu, Berry phase effects on electronic properties, Rev. Mod. Phys. **82**, 1959 (2010).

[38] T. Taychatanapat and P. Jarillo-Herrero, Electronic transport in dual-gated bilayer graphene at large displacement fields, Phys. Rev. Lett. **105**, 166601 (2010).

[39] Y. Zhang, T.-T. Tang, C. Girit, Z. Hao, M. C. Martin, A. Zettl, M. F. Crommie, Y. R. Shen, and F. Wang, Direct observation of a widely tunable bandgap in bilayer graphene, Nature (London) **459**, 820 (2009).